ARTICLE

# Chemical Scissors Tailored Nano-Tellurium with High-Entropy Morphology for Efficient Foam-Hydrogel-Based Solar Photothermal Evaporators

Chenyang Xing[1,2], Zihao Li[1,2], Ziao Wang[3], Shaohui Zhang[5], Zhongjian Xie[4], Xi Zhu[3] ✉, Zhengchun Peng[1,2] ✉

HIGHLIGHTS

- Precise exfoliation and modification of nano-Tellurium was realized by adopting a room-temperature ionic liquid as the electrolyte.

- Nano-Tellurium with high-entropy morphology can offer greater solar absorption and more kinds of surface chemical groups, giving rise to superior photothermal properties.

- Nano-Tellurium-poly(vinyl alcohol)-based photothermal foam hydrogels, with high compressibility, excellent water transport rate and low evaporation enthalpy of water, combined with a new heat-supply model, achieve an evaporation rate of $4.11 \text{ kg m}^{-2} \text{ h}^{-1}$ with energy efficiencies up to 128% under 1 sun irradiation, which are the highest values for semiconductor-based nanocomposites reported so far.

ABSTRACT The development of tellurium (Te)-based semiconductor nanomaterials for efficient light-to-heat conversion may offer an effective means of harvesting sunlight to address global energy concerns. However, the nanosized Te (nano-Te) materials reported to date suffer from a series of drawbacks, including limited light absorption and a lack of surface structures. Herein, we report the preparation of nano-Te by electrochemical exfoliation using an electrolyzable room-temperature ionic liquid. Anions, cations, and their corresponding electrolytic products acting as chemical scissors can precisely intercalate and functionalize bulk Te. The resulting nano-Te has high morphological entropy, rich surface functional groups, and broad light absorption. We also constructed foam hydrogels

based on poly (vinyl alcohol)/nano-Te, which achieved an evaporation rate and energy efficiency of $4.11 \text{ kg m}^{-2} \text{ h}^{-1}$ and 128%, respectively,
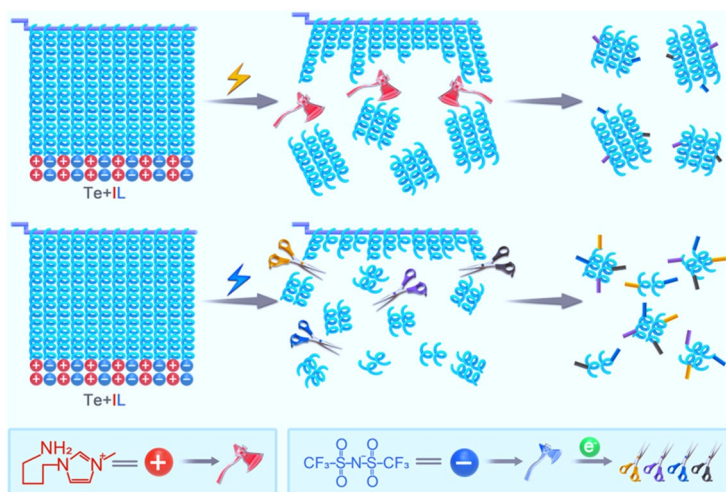
✉ Xi Zhu, zhuxi@cuhk.edu.cn; Zhengchun Peng, zcpeng@szu.edu.cn

1 State Key Laboratory of Radio FrequencyHeterogeneous Integration, Shenzhen University, Shenzhen 518060, People's Republic of China
2 Center for Stretchable Electronics and NanoSensors, College of Physics and Optoelectronic Engineering, Shenzhen University, Shenzhen 518060, People's Republic of China
3 School of Science and Engineering, The Chinese University of Hong Kong, Shenzhen, Shenzhen 518172, People's Republic of China
4 Institute of Pediatrics, Shenzhen Children's Hospital, Shenzhen 518038, Guangdong, People's Republic of China
5 International Collaborative Laboratory of 2D Materials for Optoelectronics Science and Technology of Ministry of Education, Institute of Microscale Optoelectronics, Shenzhen University, Shenzhen 518060, People's Republic of China

under 1 sun irradiation. Furthermore, the evaporation rate was maintained in the range 2.5–3.0 kg m^{-2} h^{-1} outdoors under 0.5–1.0 sun, providing highly efficient evaporation under low light conditions.

KEYWORDS Tellurium; High entropy; Electrochemical modification; Solar absorption; Evaporation rate

1 Introduction

The mono-elemental group-VIA semiconductor tellurium (Te) has drawn extensive research attention owing to its potential application in optoelectronic, photothermal, and thermoelectric devices [1–6]. Te has a narrow energy bandgap (E_g) of 0.30 eV in its bulk state. Te-based nanomaterials (nano-Te) show layer-dependent E_g values [7], similar to the group-VA element black phosphorus (BP) [8–12]. Nano-Te also exhibits both plasmonic- and Mie-type resonances [13], together with low thermal conductivity [14–16], making it a promising material for solar photothermal applications that use solar radiation over the wavelength range 250–2500 nm [17]. Recent strategies to synthesize nano-Te include chemical methods such as common redox reactions [18, 19] and hydrothermal reactions [20, 21]; biosynthesis [22, 23]; and physical methods such as liquid phase exfoliation (LPE) [24–26], physical vapor deposition (PVD) [27], and laser ablation [13]. However, nano-Te fabricated by these methods exhibits unsatisfactory solar absorption, particularly in the infrared (IR) region. This feature is partly attributed to the regular nature of Te nanostructures, i.e., zero-dimensional (0D) quantum dots (QDs) [28]; one-dimensional (1D) nanowires [29] or nanoneedles [30]; and two-dimensional (2D) nanosheets [24, 27].

Ideal solar photothermal agents (SPAs) have two main requirements: They should effectively absorb solar radiation, and they should have a high light-to-heat conversion efficiency. The former quality is closely related to the electronic structure and morphology of the SPA [31, 32], and the latter relates to its surface state, including defects, impurities, and surface termination [33]. Accordingly, for nano-Te to fulfill its potential as a solar photothermal agent, it should have multi-dimensional and diverse structures with a high specific surface area to absorb solar energy over a broad range along with an abundance of surface defects and/or functional groups to transform photoexcited electrons into heat energy. Accordingly, we aimed to develop a nano-Te material system for SPAs.

Electrochemical exfoliation (ECE) strategies have been applied for the fast and effective preparation of few-layer 2D inorganic materials, particularly for layered materials such as classic graphene and BP [34, 35]. Typically, electrolytes and solvents play an important role in intercalating and decorating the target objects [9, 36]. Recently, room-temperature ionic liquids (ILs), composed only of cations and anions, have been applied as intercalation agents to produce graphene [37–39], graphene QDs [40], BP QDs [41], and BP nanosheets [42]. Tang et al. reported the use of a fluoride-containing IL to exfoliate BP crystals in an electric field [41, 42]. In this strategy, the BF$_4^-$ anions decomposed into F$^-$, which chemically bind with the BP surface. Consequently, both air stability and light absorption of the IL-modified BP were improved.

Both the cations and anions in ILs can be electrolyzed in an electric field [43–49]. For instance, IL imidazolium cations can be electrolyzed into imidazolium radicals [44] and even alkyl radicals [50]. Interestingly, the bis[(trifluoromethyl) sulfonyl]imide (NTf$_2$) anions can be electrolyzed into several active species [43], including the radical •NSO$_2$CF$_3^-$ and the anions SO$_2$CF$_3^-$, NSO$_2^-$, SO$_2^-$, CF$_3^-$, and even F$^-$. By these means, metal fluorides can be formed on electrodes [51–53]. Based on these previous findings, these chemical species have the potential to act as electrolytes and participate in exfoliation procedures. Furthermore, for newly exfoliated nanomaterials, where physical interactions between sheets or chains have been broken, there are transiently and highly reactive surfaces. If active electrolyzed species are present in the ECE system, new nanomaterials may be readily grafted to them, giving rise to surface-decorated Te nanomaterials if bulk Te is used as a working electrode. Such an unique preparation of Te-based nanomaterials by ECE of Te has not been reported previously [54]. Therefore, an ECE strategy featuring electrolyzable ILs as electrolytes may be expected to provide functional nano-Te from bulk Te under electrochemical conditions.

In this work, for the first time, we report the electrochemical synthesis of nano-Te with the use of an electrolyzable ionic liquid [1-aminopropyl-6-methylimidazolium]

{[bis(trifluoromethyl)sulfonyl]imide}, [C$_3$NH$_2$MIm][NTf$_2$], as the electrolyte. By adjusting the applied voltage, precise exfoliation of Te by IL anions and/or cations realizes a wide variety of Te morphologies owing to the different exfoliation mechanisms of the IL components. Anion-induced nano-Te has a varied morphology, which increases solar absorption, and provides tunable water-stability for at least 14 days in water. Accordingly, this form of nano-Te was used as a photothermal nanofiller in poly (vinyl alcohol) (PVA)-based foam hydrogels generated by a foam phase conversion strategy. These PVA/nano-Te foam hydrogels combine the advantages of a foam (high porosity, high water transport, excellent solar absorption, and photothermal efficiency) and a hydrogel (low water evaporation enthalpy). Thus, excellent evaporation performances under 1 sun (indoor) and weak light irradiation (outdoor) conditions were achieved.

2 Experimental and Calculation

2.1 Fabrication Strategies

2.1.1 Electrochemical Strategy

The nano-Te materials were fabricated using a classic two-electrode electrochemical method with an electrolyzable ionic liquid [1-aminopropyl-6-methylimidazolium] {[bis (trifluoromethyl) sulfonyl] imide}, [C$_3$NH$_2$MIm][NTf$_2$], as the electrolyte (0.5 M). In brief, commercial bulk Te crystal was used as working electrode while Pt as the counter one, and acetonitrile (CH$_3$CN) as the solvent. Bias potential, including positive $+1, +2, +3, +4,$ and $+5$ V, and negative $-1, -2, -3, -4,$ and -5 V, was applied onto Te electrode. After a certain time of exfoliation, the nano-Te/CH$_3$CN colloidal solution was obtained, followed by centrifuged at 200 rpm for 10 min to remove unexfoliated bulk Te, filtration, washing with CH$_3$CN, methanol, and water. The final solid nano-Te can be obtained by freeze-drying operation.

2.1.2 Fabrication of PVA-Based Hydrogels and Foam Hydrogels

PVA Hydrogel Typically, PVA solution, glutaraldehyde (GA), HCl solution, and deionized (DI) water were fully mixed at 0 °C (with a moderate stirring rate of 500 rpm), followed by a heating process at 40 °C for 10 min to get gelation. The final PVA hydrogels were obtained by fully dialyzing them with water at room temperature.

PVA Foam Hydrogel Differed from the above method of PVA hydrogel, the PVA foam hydrogel precursor was first fully foamed by using a high stirring rate of 35,000 rpm at 0 °C after its fully mixing under low stirring speed. Then, a similar heating cross-linking strategy was used to stabilize the foamy system, followed by being frozen at −20 °C for 1 h and thawed at room temperature. The final PVA foam hydrogels were obtained by repeatedly squeezing them in hot water to replace the bubble-introduced air with water.

PVA/F-127 Foam Hydrogel To further homogenize and stabilize the bubbles in PVA system, nonionic surfactant PEO$_{106}$-PPO$_{70}$-PEO$_{106}$ (commercial name: Pluronic F-127) was used and its solution with a 100 mg mL^{-1} concentration was used to replace the above DI water. Similar procedures can obtain the PVA/F-127 foam hydrogels.

PVA/F-127/Nano-Te Foam Hydrogel The as-prepared nano-Te was introduced into the PVA/F-127 system to act as solar absorbent and photothermal nanofiller. Prior to foaming, the nano-Te was thoroughly mixed with PVA/F-127 system to get a homogeneous state. PVA/F-127/nano-Te foam hydrogels with various nano-Te concentrations can be obtained according to the above preparation strategy.

2.2 Characterization

Nano-Te The morphology was characterized by using transmission electron microscopy (TEM) with a type of Tecnai G2, Spirit120kV. The surface termination was detected by X-ray photoelectron spectroscopy (XPS) and Fourier-transform infrared spectroscopy (FTIR), respectively. The crystalline behaviors were recorded by X-ray diffraction (XRD), and the vibration behaviors were analyzed by Raman spectra. The solid solar absorption property was measured by using an instrument from 200 to 2500 nm.

Foam Hydrogels The cross-section morphology was observed by using scanning electron microscopy (SEM). Before testing, a thin of Pt layer was sprayed onto the surface of samples to improve their conductivity. The porous property of samples was evaluated by recording their pore size distribution and porosity by using mercury intrusion method.

The water transport and retain property were tested by testing water absorption rate within certain time after absorbing water and water mass after centrifugation after 2500 rpm for 10 min, respectively. The solar absorption behaviors were calculated by deducting the transmittance and reflections of samples at seawater wet and dry forms. The water evaporation enthalpy was measured by calculating the mass loss of water in samples under certain conditions that has dark conditions. The mechanical properties were evaluated by testing their compressibility as a frequency of 2 s^{-1} at a fixed compressive ratio of 85%.

Indoor and Outdoor Solar Desalination Foam hydrogels were inserted into the white heat-insulative foam or black heat-absorption foam, namely thermal isolation model and heat-supply model, respectively, to construct the solar evaporators. Owing to their self-floating property of both foam hydrogels and foams, these evaporators were floating onto the seawater surfaces. The mass and surface temperature changes of the systems were recorded by using electron balances and infrared thermal imager during evaporation procedure at room temperature. The simulated light was fixed at one sun by calibrated by using an optical power meter before use. The evaporation rate (ν) and energy efficiency (η) were calculated by using the following equations. At least three samples were used to report the average value. The real seawater was obtained Shenzhen Bay, Shenzhen, China, and was used after a simple filtration to remove any of visible floating objects.

In outdoor, the large-scale solar evaporators with same volume ratios as the one indoor were evaluated from 8:00 am to 18:00 pm every day during period from September 4, 2022, to October 6, 2022. At every critical time data, the ν, surface temperature, ambient temperature, and solar light intensity were recorded. For instance, at 8:00 am, the ν indicates the average value between the time 7:00 am and 8:00 am. Another sample, at 9:00 am, the ν indicates the average value between the time 8:00 am and 9:00 am. Except the rainy day and partly of rainy day at one day, 32 days and 341 data of every time point were continuously detected.

All calculations based on density functional theory (DFT) were utilized through the Vienna ab initio simulation package (VASP) [55]. Interactions arising from exchange correlation were depicted through the generalized gradient approximation (GGA) configured by the Perdew–Burke–Ernzerhof (PBE) approach [56]. The DFT-D3 scheme facilitated the inclusion of van der Waals (vdW) interactions [57, 58]. The energy threshold of the plane wave base was defined at 500 eV, with a $3 \times 3 \times 1$ k point grid sampled through the Monkhorst–Pack technique ensuring sufficient precision for Brillouin zone integration [59]. The conjugate gradient (CG) algorithm enabled complete relaxation of all structures until a force less than 0.005 eV/Å and an energy fluctuation under 10–8 eV were achieved. To emulate the surface of Te, we adopted a $2 \times 2 \times 1$ monolayer supercell and sliced the crystal along the (0 0 1) orientation. The vacuum domain in the z-direction was prescribed at 15 Å to preclude inter-layer interactions. Different vibrational modes of adsorbate groups were simulated by changing corresponding bond length.

The adsorption energies (E_{ads}) were calculated by:

$$E_{\text{ads}} = E_{\text{ad}} + E_{\text{slab}} - E_{\text{ad+slab}} \tag{1}$$

where E_{ad}, E_{slab}, and $E_{\text{ad+slab}}$ represent the total energy of the adsorbate, the relaxed slab, and the slab adsorbed by the adsorbates, respectively.

3 Results and Discussion

3.1 Entropy and the Photothermal Effect

The temperature of this system can be modeled with a two-slab model as reported by Gartner [60], in which the temperature distribution between two infinite semiconductor slabs is calculated. One of the slabs is illuminated and heat is transferred between the slabs. The temperature at the illuminated slab is T_1, and the temperature at distance w is denoted as T_2. The solution for T_1 is given as:

$$T_1 = -\left\{ \alpha T_0 - \frac{\kappa}{w} T_2 + f_{\text{AC}} \left[1 - \frac{L}{\tau w} \times \frac{2D - (D - s_2)e^{-W} - (D + s_2)e^{W}}{(D + s_1)(D + s_2)e^{W} - (D - s_1)(D - s_2)e^{-W}} \right] \right\} \times \left(\frac{\kappa}{w} - \alpha \right)^{-1} \tag{2}$$

where α is a constant for the heat emitted via radiation; κ is the thermal conductivity of the material; f_{AC} is the radiated flux absorbed exclusively under carrier generation in the bulk or on the surface of the sample; D is the ambipolar diffusion constant given by $(n + p)/(n/D_p + p/D_n)$ with n, p, D_n, D_p relating to the concentrations and diffusion constants of the electrons and holes; L is the diffusion length of excess pairs as $\sqrt{D\tau_p}$ with τ_p as the lifetime of holes; and $\mathcal{D} = D/L, W = w/L, s_1, s_2$ are the recombination velocities of the illuminated slab and the other slab. The shape of this function is determined by the reciprocal terms on T_2 and on the outside, which have a singularity at $w = \kappa/\alpha$. Thus, when using this theory, the range where w approaches this singularity is invalid.

We now consider the size distribution effect, i.e., the entropy effect. Suppose that the distribution is identical for N particles of the same $w = w_0$, the T_1 value of this distribution is:

$$T_1^{\text{identical}} = \sum_{i=1,\dots,N} T_1(w_0)\frac{1}{N} = T_1(w_0) \qquad (3)$$

Assuming that the distribution is Gaussian with mean w_0 and standard deviation σ, the T_1 value is described by a Gaussian function as:

as chain-like structures with weak van der Waals interactions between chains allowing them to be broken by external force. The IL is composed of anions and cations, which can both interact with the Te chains under an electric field in the electrolyte. Therefore, by adjusting the electric field direction, cations or anions from the IL can be selectively interacted with the bulk Te. Note that the IL used here, $[C_3NH_2MIm][NTf_2]$, can be electrolyzed or decomposed into several active species, including radicals and anions. Hence, there are many modes of physical exfoliation and chemical bonding with Te.

At an applied potential of $+5$ V to the Te electrode (Fig. S3) (Movie S1), exfoliation of Te is observed within approximately 2 s, while bubbles appear at the surface of the Pt counter electrode, which were determined not to originate from the electrolysis of water or CH_3CN(not shown here). At 5 s (Fig. 1c), filament-like black products are clearly observed at the Te electrode. The expanded volume of Te indicates successful intercalation of the IL. Prolonged exfoliation improves the yield of this product (labeled nano-Te @ $+5$ V) (Fig. 1d), which finally presents as a deep black colloidal solution in CH_3CN (Fig. S3). Notably,

$$T_1^{\text{Gaussian}} = \int_{w_t=0}^{w_t=\infty} T_1(w_t) \frac{1}{\sqrt{2\pi\sigma^2}} e^{-\frac{1}{2}\left(\frac{w_t-w_0}{\sigma}\right)^2} dw_t \approx \frac{T_2\kappa\left(2\alpha^2\sigma^2 + 5(\kappa - \alpha w_0)^2\right) - T_0\alpha\left(5\kappa^2 w_0 + 5\alpha^2 w_0^3 + 2\alpha\kappa(\sigma^2 - 5w_0^2)\right)}{3\sqrt{2\pi}(\kappa - \alpha w_0)^3} \qquad (4)$$

According to the numerical values in Gartner's model [60] and other publications [61–63], the numerical parameters may be taken as $S_1 = 100$ cm s^{-1}, $S_2 = 100$ cm s^{-1}, $T_1 = 298$ K, $T_2 = 358$ K, $\mathcal{D} = 50$ cm^2 v^{-1} s^{-1}, $L = 1$ cm, $\tau = 0.02$ s, $f_{ac} = 0.01$ W cm^{-2}, $\kappa = 0.5$ W K^{-1}, $\alpha = 2$ W K^{-1}, $\sigma = 0.001$ cm, and $w_0 = 0.002$ cm. Hence, the entropy effect can be calculated as shown in Fig. S1. The Gaussian distribution significantly increases the temperature T_1, which means that high-entropy semiconductors are likely to have greater photothermal effects.

3.2 Electrochemical Exfoliation of Te

To fabricate high-entropy Te semiconductors, a common electrochemical exfoliation strategy was used. A bulk Te crystal was selected as a working electrode and fixed onto a Pt clamp, and another Pt sheet was used as a counter electrode (Fig. S2). As illustrated in Fig. 1a, b, bulk Te exists

when the electric field polarity at the Te electrode is changed (i.e., -5 V, Fig. S3) (Movie S2), several distinct phenomena occur. First, the Te electrode exhibits slow exfoliation (from approximately 5 s) (Fig. 1e) and the exfoliated products float on the electrolyte surface (from approximately 15 s) (Fig. S3).

Finally, a clear two-phase interface is formed (at approximately 300 s) (Fig. 1f). A prolonged reaction time also increases the yield. In this case, no bubbles are observed at the Pt counter electrode, instead appearing at the Te working electrode. Similarly, the as-prepared Te products, denoted nano-Te @ -5 V, appear black in CH_3CN (Fig. S3). However, the corresponding filtered solutions of the above two products have different colors (Fig. S4). In addition, the exfoliation of bulk Te, under either positive or negative bias, had a threshold potential at approximately $+3$ and -3 V, as shown in Figs. 1g, h and S5, respectively. On exceeding these
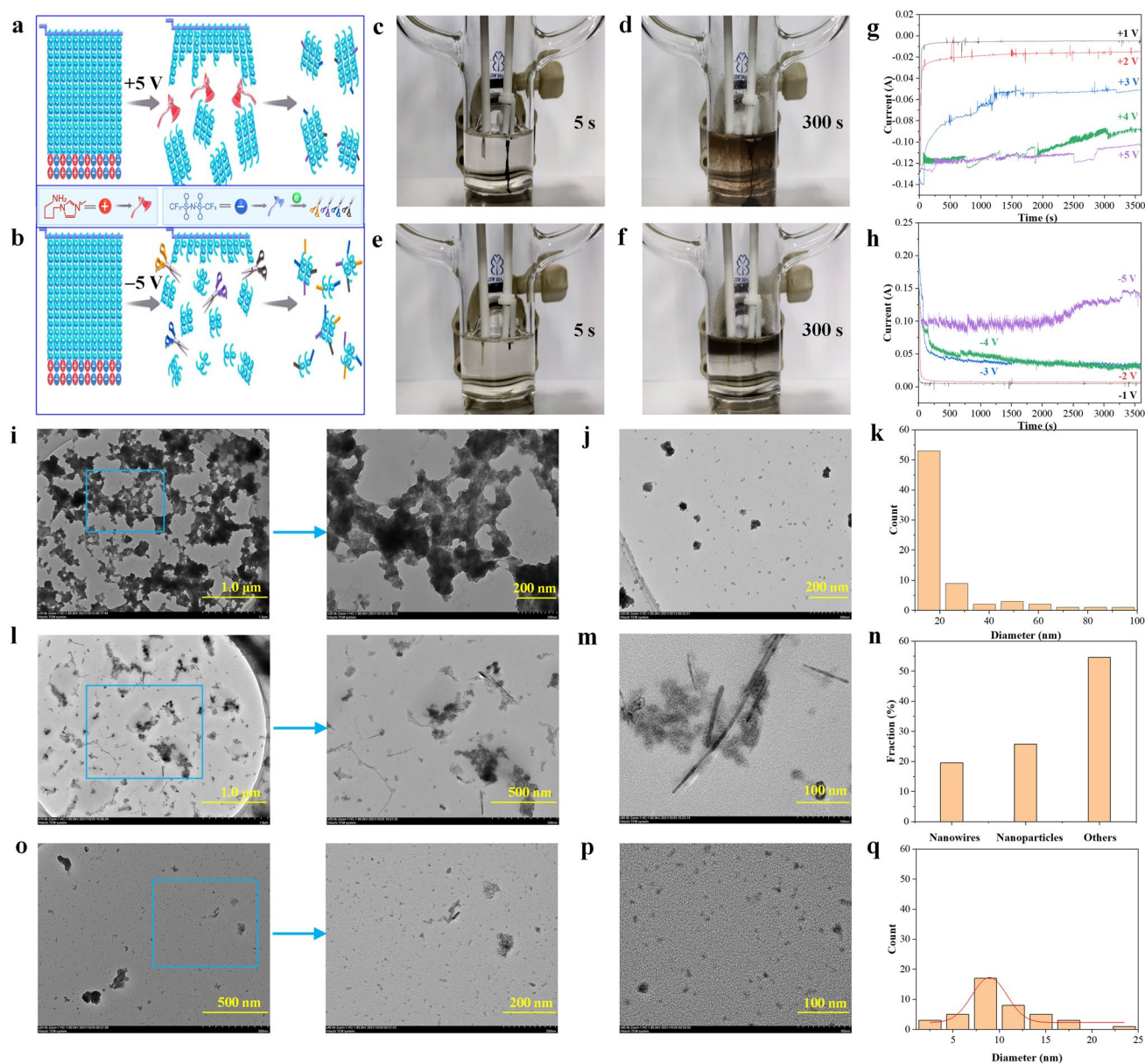
Fig. 1 IL-assisted precise electrochemical synthesis of nano-Te. **a, b** Schematic of the intercalation and exfoliation of bulk Te by IL ions and their corresponding electrolyzed active species under opposite polarities. A typical standard two-electrode setup, including a Te crystal working electrode and high-purity Pt counter electrode for electrochemical modification of **c, d** Te under + 5 V or **e, f** − 5 V bias potentials. **g, h** Exfoliation current versus time in the preparation of nano-Te under various applied voltages. Typical TEM images and size distribution of nano-Te obtained from Te electrodes **i–k** at + 5 V and **l–q** at − 5 V

threshold potential values, the absolute values of exfoliation current start to increase sharply with applied potential. The chemical stability of the as-prepared nano-Te @ − 5 V in water was evaluated simply by observing its color change. As shown in Fig. S6, the bare nano-Te@ − 5 V

shows moderate stability for 7 days before showing clear degradation at 14 days. In contrast, glutathione (GSH)-modified nano-Te exhibits stability in water for 14 days, indicating that the stability of nano-Te@ − 5 V may be modified with the use of appropriate polymers.

3.3 Morphologies of Nano-Te

The microstructures of the nano-Te samples were evaluated by TEM imaging, as shown in Fig. 1i–q. The nano-Te @ + 5 V shows porous and continuous structures (Fig. 1i). The pore sizes are the range of 20–300 nm with irregular morphologies (Fig. 1i). The high-magnification image in Fig. 1j also shows the presence of 0D nanoparticles with diameters of 10–30 nm (Fig. 1k). Conversely, nano-Te @ − 5 V shows a wide variety of different architectures, as shown in Fig. 1l, m. 1D nanofibers (20%) with lengths of 100 nm to 1.0 μm, 0D nanoparticles (26%), and other nanostructures (54%) are observed (Fig. 1n). In addition, smaller 0D nanoparticles (Fig. 1o) and even quantum dots (QDs) (Fig. 1p, q) can also be observed. Exfoliation of nano-Te at + 5 V is rapid and produces particles with relatively large dimensions. The macroscopic filament-like appearance (Fig. 1c) is reflected by a continuous microscopic structure (Fig. 1i). However, in the case of the sample prepared at − 5 V, the exfoliation proceeds slowly such that small nano-Te microstructures are formed, resulting in the biphasic mixture observed (Fig. 1f). Owing to the chain-like structure of Te, the nano-Te materials feature continuous structures for the + 5 V sample and 1D nanofibers for the − 5 V sample. The nano-Te @ − 5 V sample shows a more diverse variety of morphologies, i.e., high-entropy morphology, which may be beneficial for its application to solar desalination.

3.4 Physical Properties of Nano-Te

Relative to bulk Te, nano-Te obtained at + 5 or − 5 V features similar Raman characteristics (Fig. 2a) and crystalline properties (Fig. 2b). No crystalline TiO_x is observed in these measurements [64–66]. However, TiO_x is detected by FTIR and XPS characterizations. For instance, bulk Te exhibits weak absorption (Fig. 2c) and clear high-valence Te-element signals (Fig. 2g), indicating a trace amount of TiO_x on its surface, probably because of oxidation in air. Interestingly, such TiO_x could absorb water molecules from the air to produce a strong hydrogen-bind interaction, as reflected by the strong absorption at 3334.6 cm^{-1} (Fig. 2d). For the nano-Te samples, apart from the strong Te–O bond, other weak functional groups are observed (Fig. 2c). In its pure form, the IL used exhibits absorption peaks at 763.2 cm^{-1} (CF$_3$) [67], 1049.6 cm^{-1} (δ_{as}-S–N–S) [67–69], 1130.1 cm^{-1}

(ν^S-SO$_2$) [68, 69], 1173.9 cm^{-1} (ν_{as}-CF$_3$) [43], 1345.1 cm^{-1} (ν_{as}-SO$_2$) [67], and similar peaks are observed in the nano-Te spectra, in particular for nano-Te @ − 5 V. The characteristic absorptions for the imidazolium ring at 1567.4 cm^{-1} (ν N1C2N3) [68] and 1575.6 cm^{-1} (ν C = C) [70] are not observed in the nano-Te samples (Fig. 2c). However, clear alkyl C–H absorption peaks are observed at 1463.7 cm^{-1} (δ_s CH$_3$) (Fig. 2c), 2852.2, 2921.6, and 2956.3 cm^{-1} in Fig. 2d, which are ascribed to CH$_2$ vibration [67–69, 71] when compared with that of the pure IL used (Fig. 2d), suggesting that alkyl side chains instead of imidazolium ring may graft onto the nano-Te surfaces. These FTIR results indicate that the two types of nano-Te are both terminated by the fragmented chemical groups originating from the electrolyzed anions in the IL. Furthermore, nano-Te @ − 5 V appears to bear more functional groups in view of the presence of relatively strong peaks.

This surface chemical modification was further confirmed by the XPS measurements, as shown in Fig. 2e–g. Both nano-Te samples contain some F, and these peaks are relatively intense for nano-Te @ − 5 V compared with those for nano-Te @ + 5 V (Fig. 2e). Signals from N are also observed in a broad shoulder peak for both nano-Te samples (Fig. 2f). The above F and N signals are not found for bulk Te, indicating they originate from the IL. Additionally, the broad N peak can be deconvoluted into two possible peaks, which may be assigned to N from the anion and N from amino groups in the side chains from the imidazolium ring, considering that the N from imidazolium cations has a higher binding energy (> 400 eV) relative to that of anions [72–74]. Furthermore, both nano-Te samples show the presence of S at a lower binding energy (Fig. S7). Bulk Te also contains some S, which may be attributed to S doped into the commercial bulk Te. The above XPS results suggest that both nano-Te samples contain F-, N-, and S-containing chemical groups, which is in good agreement with the FTIR results.

The UV–Vis–NIR absorption spectra of the nano-Te samples recorded in CH$_3$CN are shown in Fig. 2h. In the case of nano-Te @ − 5 V obtained after 500 rpm centrifugation, two distinct absorption peaks at 238 and 589 nm are observed, which can be attributed to the allowed direct transition from the valence band (VB) to the conduction band (CB) and an indirect forbidden transition, respectively. Furthermore, on elevating the centrifugation speed to 1000 and 2000 rpm, the first direct VB→CB transition absorption remains unchanged; however, the second forbidden indirect transition absorption is
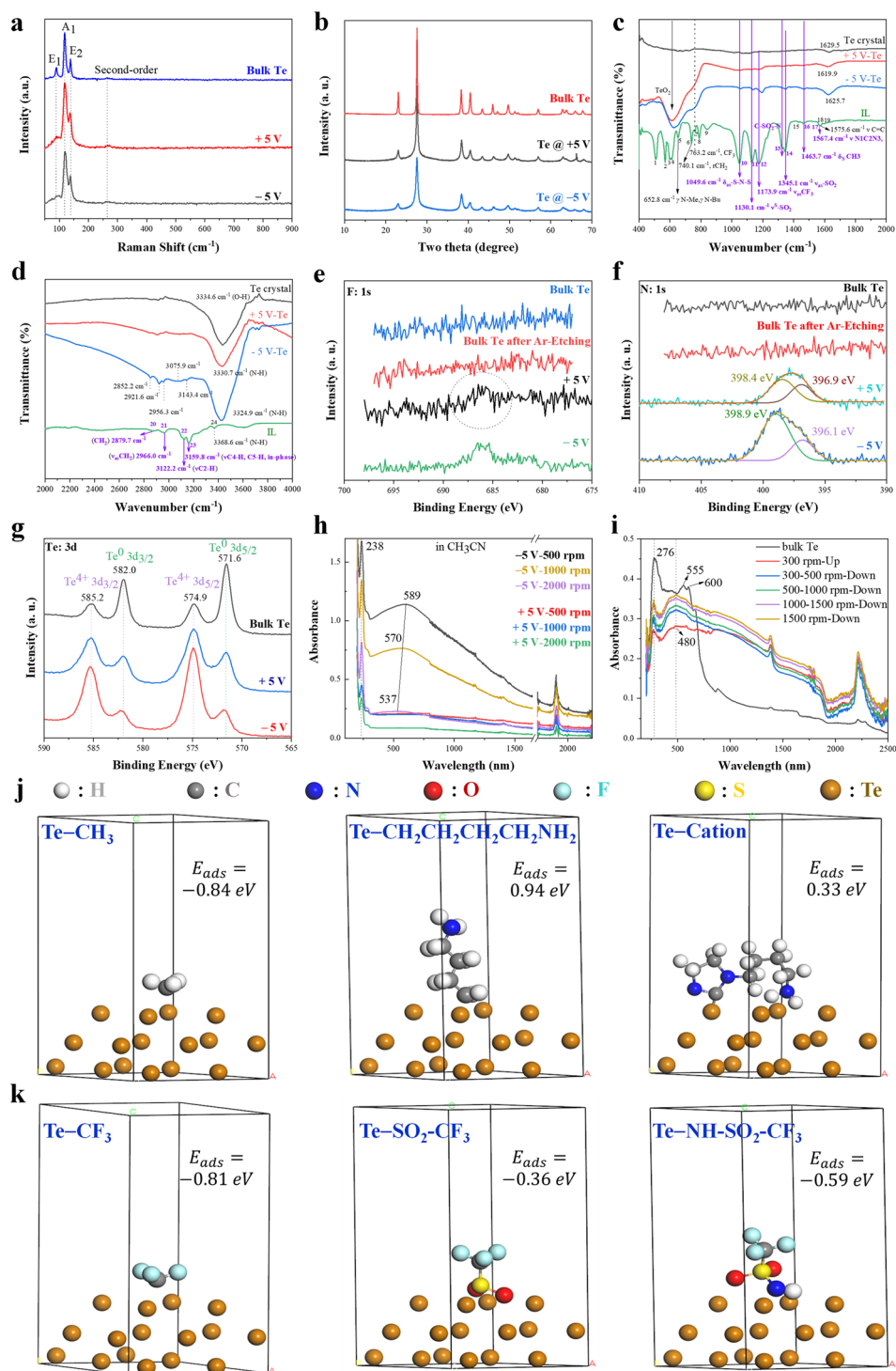
Fig. 2 Physical properties of bulk Te and nano-Te samples under different conditions. **a** Raman spectra; **b** XRD patterns; **c–d** FTIR spectra; **e–g** XPS for **e** F, **f** N and **g** Te elements. Light absorption spectra of **h** nano-Te samples in CH_3CN and **i** a solid nano-Te @ −5 V sample over the solar spectral region. **j, k** Atomic structures and the corresponding adsorption energy of specific functional groups terminated Te at 001 face

blue-shifted and has lower intensity. These unique absorption behaviors can be attributed to the diverse morphologies and dimensions of nano-Te @ − 5 V, which has high-entropy morphology. Therefore, relative to the samples obtained at high centrifugation speeds, those obtained at lower centrifugation speeds are more diverse in morphology, which provides better and broader optical absorption in the visible-light region. Regrettably, the nano-Te @ + 5 V sample, which has larger continuous microstructures, exhibits lower absorption of visible-IR light. Figure 2i shows the light absorption behaviors of the solid nano-Te @ − 5 V samples from different fractional centrifugation components. The solid bulk Te also presents two absorption features, a sharp peak at 276 nm and another broad peak in the range 555–600 nm, assigned to the two aforementioned transitions. However, bulk Te has poor optical absorption in the region 600–2500 nm. Nano-Te @ − 5 V samples from different fractional centrifugation components show broad absorption. Thus, nano-Te @ − 5 V has a broader solar absorption capacity than that of bulk Te. A combination of samples from centrifugation portions obtained in the range 300–1500 rpm (Fig. 2i) shows excellent optical absorption similar to that for the sample obtained at 500 rpm (Fig. 2h).

3.5 Mechanism of Exfoliation and Functionalization of Te

Previous studies have revealed that ILs can be electrolyzed at potentials over their electrochemical windows [42–48]. Furthermore, NTf$_2$ anions can be reductively and successively decomposed into several active species, such as $\bullet NSO_2CF_3^-$, $SO_2CF_3^-$, $NSO_2CF_3^-$, SO_2^-, and CF_3^- [43, 48], and can also be electrooxidized into NTf$_2\bullet$ [75, 76]. The gaseous product CHF$_3$ indicates reductive degradation of NTf$_2$ anions. Furthermore, fluoride is also detected on the surfaces of the electrodes (LiF and MgF$_2$) [51–53]. Imidazolium cations can be reductively transformed into dimers and alkyl radicals [50, 77], and these products are more colored in solution relative to those from NTf$_2$ anions [78]. The density functional theory (DFT) calculation for the adsorption energies (E_{ads}) of the aforementioned specific chemical functional groups onto the Te surface is shown in Fig. 2i, k, respectively. The − CH$_3$ (E_{ads} = 0.84 eV) and − NH$_2$ (E_{ads} = 0.71 eV) groups, the partial side chains of the imidazolium cations, were found to have a potential to chemically bond with Te due to their negative E_{ads} values. However, the whole imidazolium cation

ring with an E_{ads} value of 0.33 eV cannot graft onto the Te. On the other word, the anion-induced groups of −CF$_3$, −SO$_2$–CF$_3$ and –NH–SO$_2$–CF$_3$ were calculated to be able to link with Te. Additionally, other groups such as − F (from the further reduction of − CF$_3$) (E_{ads} = − 0.93 eV) and − OH (from H$_2$O) (E_{ads} = − 0.67 eV) can also bond with Te. These simulation results are very good agreement with the above FTIR and XPS results.

Based on previous reports and our experimental findings, we propose the following possible delaminating mechanism for Te: (1) Upon applying an electric field, the anions and cations of the IL move to the corresponding electrodes. Their distribution may follow the Gouy–Chapman–Stern model, wherein cation–anion interactions (hydrogen–bond and electrostatic interactions) [79, 80], cation/anion–Te electrode adsorption interactions [81], and cation/anion–CH$_3$CN hydrogen–bond interaction [82–84] need to be considered. Therefore, the possibility that both imidazolium cations and their counter NTf$_2$ anions coexist on the Te or Pt electrodes cannot be overlooked [85]. (2) Specifically, taking into account the delamination current behavior illustrated in Fig. 1g, h, at + 5 V, Te is the cathode and Pt is the anode, and the imidazolium cations migrate to the Te electrode and, together with their reduction products, intercalate into Te crystals. Their large size and organic nature make the as-prepared nano-Te macroscopically and also microscopically large and flexible (probably forming cation-Te complexes) in CH$_3$CN and provide faster Te stripping. Their steric bulk is also responsible for the difficulty in delaminating nano-Te with imidazolium-based products as compared with alkyl-side-chain-based radicals. At the Pt electrode, the anions aggregate and take place in multi-step electrochemical reactions, finally resulting in CHF$_3$ [49]. The possible cation–Te complexes on the Te surface may hinder the reaction of nano-Te with the formed F-containing species, thus resulting in nano-Te with weak F signals (Fig. 2e). (3) In sharp contrast, at − 5 V, Te acts as the anode and Pt as the cathode. In this case, NTf$_2$ anions accumulate near the Te and decomposition reactions occur, generating a series of active species that intercalate, strip, and chemically graft to Te. Interestingly, these inorganic species are smaller in both size and momentum, thus providing a slower rate of Te delamination and producing nano-Te in the form of small-sized fragments that float to the electrolyte surface. Possibly, because these species may have energy and volume matching with the surface of different-dimensional Te, the resulting nano-Te

materials have multi-morphology and multi-dimensional high-entropy properties.

3.6 Nano-Te-loaded PVA-based Foam Hydrogels

To realize the application of nano-Te to solar interfacial desalination, PVA-based foam hydrogels were explored as a model platform. As shown in Fig. 3a, by virtue of the excellent foaming ability of the PVA solution, we developed a foam phase inversion strategy to fabricate PVA/F-127/nano-Te foam hydrogels in which F-127, a triblock copolymer, acts as the foam stabilizer. We envisioned that these foam hydrogels would combine the performance characteristics of both foams and hydrogels. Briefly, the pre-mixed homogeneous PVA/F-127/nano-Te solutions were subjected to a high-speed rotation treatment (35,000 rpm, 180 s), generating a foam (Fig. S8). The addition of F-127 further homogenized and stabilized the foam. The foaming procedure was completed within 180 s and subsequent cross-linking between PVA and glutaraldehyde fully stabilized the hydrogel.

Figure 3b shows PVA/F-127/nano-Te precursor solutions having different nano-Te concentrations. Upon foaming (Fig. 3c), the volume of all the solutions increases at least twofold. Following heat treatment to initiate cross-linking, these volumes are effectively maintained (Fig. 3d). At this stage, the foam hydrogels are filled with air, so water is introduced to the pores by simple compression in water.

Typical cross-sectional morphologies of the PVA-based foam hydrogels are shown in Fig. 3e–j. Continuous and open pores are observed in the case of the PVA foam hydrogel without the addition of F-127 (Fig. 3e). Similar multi-porous structures are present in the PVA/F-127 foam hydrogels (Fig. 3f), indicating that these pores are mainly generated by the foaming conditions. Loading the PVA/F-127 foam hydrogel with nano-Te does not significantly affect its microstructure, regardless of the concentration of nano-Te (Fig. 3g–j). C, O, and Te elemental mapping images of the PVA/F-127/nano-Te sample (Fig. 3k) indicate the homogeneous dispersion of nano-Te within the foam hydrogels.

Polymeric foams are able to take up and rapidly transport large amounts water as well as exerting an anti-salting effect owing to their large open pores; however, this structure has no effects on the ΔH_E of water, which leads to low evaporation rates. Polymeric porous hydrogels can decrease ΔH_E and provide excellent water transport; however, these structures are limited by residual salt and/or dyes present in the water system when they are cleaned. Our PVA/F-127/nano-Te foam hydrogels have the aforementioned advantages of porous hydrogels while overcoming their limitations. As shown in Fig. 4a, the neat PVA foam hydrogel shows mainly large pores in the range of 10–100 μm with fewer smaller pores of several-micrometers diameter. Through the introduction of F-127 and both F-127 and nano-Te, the pores are enlarged. In addition, several pores in the range of 1–10 μm are also observed, indicating multiple pore sizes within these foam hydrogels, which is in good agreement with the TEM results. The foaming of PVA in foam hydrogels also results in its depression of crystallization (Fig. S9). The corresponding porosities of the PVA/F-127/nano-Te foam hydrogels are plotted in Fig. 4b. The PVA/F-127/nano-Te foam hydrogels show a high porosity of over 95%, similar to those of neat PVA foam hydrogel (94%) and the PVA/F-127 foam hydrogel (96.7%), respectively. The highly poly-porous structures of the foam hydrogels also result in fast water uptake, short equilibration time, and high water absorption (Fig. 4c). For example, a foam hydrogel with 0.37 wt% nano-Te can absorb ~ 2000 wt% water relative to its fully dried state within 10 s before saturating within another 10 s at a water uptake of 2750 wt%, as is consistent with typical foams. The results for all the samples are similar over the initial stage (0–10 s), where the water uptake velocity of the foam hydrogels is largely independent of the concentration of nano-Te.

The water transport and heat management within the porous foam hydrogels were also investigated by COMSOL simulations. By building meshing patterns, 2D transport velocity patterns of liquid water and wet air in the interconnected pores (overlapping circles in the COMSOL model) were generated (Fig. 4d). Capillary pressures drive water upward through linked pores, where it evaporates at the top surface under 1 sun solar energy. The water and vapor transport channel are almost a straight line owing to the high degree of pore interconnectivity, indicating negligible diffusion barriers. For the hydrogel samples with different Te loadings, the calculated total water and vapor transport velocities are shown in Fig. 4e, and they indicate that the addition of Te has little effect on the water transport properties of the PVA foam hydrogels. These results agree well with the water uptake velocity results shown in Fig. 4c.
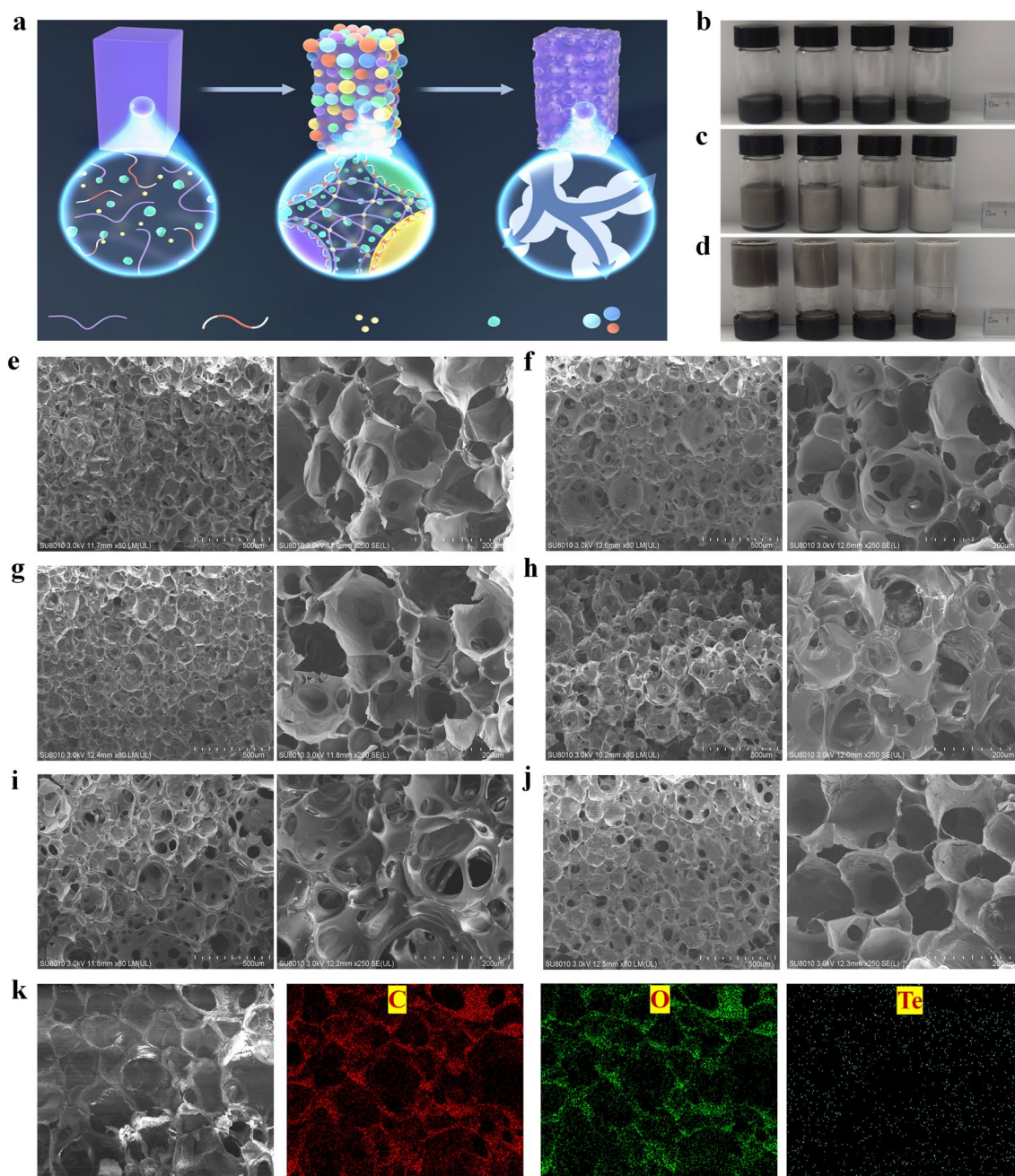
Fig. 3 Construction of PVA/nano-Te-based foam hydrogels. **a** Schematic showing the formation of foam hydrogels, including homogeneous precursor solutions (PVA, F-127, nano-Te, GA, and HCl) (first step), foaming and cross-linked state (second step), and water-filled state (third step). Photographs of PVA/F-127/nano-Te foam hydrogels at the above corresponding stages, including **b** homogeneous precursor solution with various Te contents (from left to right: 0.37, 0.19, 0.09, and 0.05 wt%), **c** fully foaming state, and **d** heat-induced cross-linked state. SEM images showing the cross-sectional microstructures of **e** neat PVA foam hydrogel, **f** PVA/F-127 foam hydrogel, and **g–j** PVA/F-127/nano-Te foam hydrogels with nano-Te contents of **g** 0.05, **h** 0.09, **i** 0.19, and **j** 0.37 wt%. **k** Elemental mapping images of C, O, and Te for the 0.37 wt% Te sample

Additionally, a simple heat-transfer model was used to describe the temperature distribution in the Te-0.05wt%-doped sample (Fig. 4f). The steady-state temperature distribution simulation predicted that the maximum temperature in the Te-0.05wt%-doped sample was 315 K at the surface of the polymeric network. This predicted value was
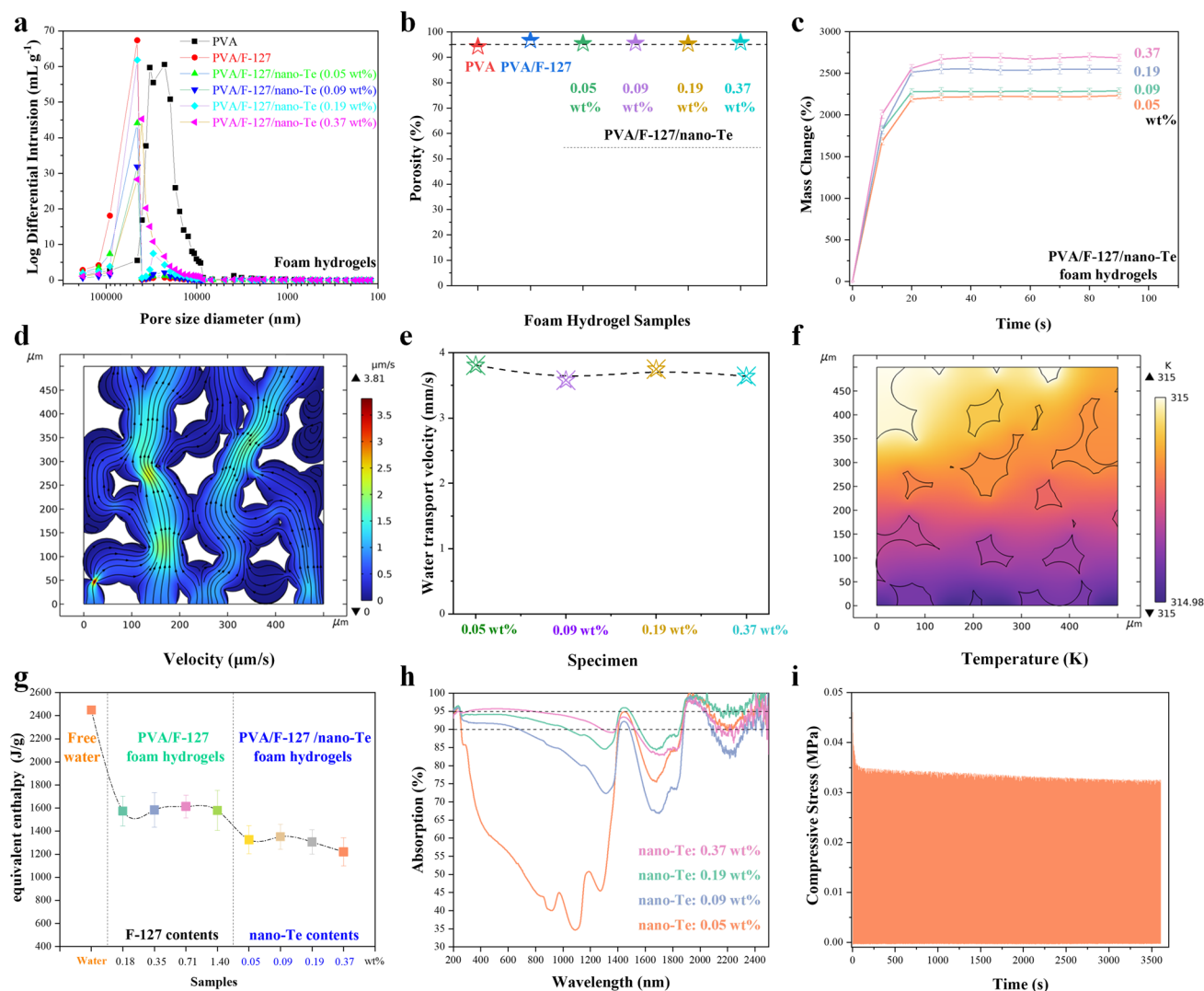
Fig. 4 Combined features of the PVA/F-127/nano-Te foam hydrogels. Foam characteristics: **a** Pore size distribution by mercury intrusion method, **b** corresponding porosity, and **c** water uptake behaviors at room temperature. COMSOL models: **d** water and wet air transport behaviors by meshing effect, **e** corresponding Te content dependence of water transport velocity, and **f** heat energy distribution under 1 sun radiation. Hydrogel characteristics: **g** evaporation enthalpy of free water and water within the foam hydrogels. **h** Solar absorption spectra of seawater-wetted foam hydrogels with various Te contents. **i** Mechanical compressive stability of a sample with 0.37 wt% Te at a fixed compressive ratio of 85%

close to our experimental value (see below), confirming the heat confinement effect of Te doping. The PVA-based foam hydrogels had a considerably lower value of ΔH_E for water evaporation, as shown in Fig. 4g. The experimental ΔH_E value (obtained by using a previously reported method) of approximately 1200 J g^{-1} observed in the case of the PVA/F-127/nano-Te foam hydrogel with 0.37 wt% nano-Te is half that of free water. The other PVA/F-127/nano-Te foam hydrogels also show decreased ΔH_E values that are superior to those of PVA/F-127 foam hydrogels without nano-Te. The

highly porous structures of these foam hydrogels, particularly with the addition of nano-Te, which influences the pore distribution and effectively elevates the fraction of intermediate water, may be responsible for the decreased ΔH_E value [86].

Figure 4h shows the solar absorption behaviors of seawater-wetted PVA/F-127/nano-Te foam hydrogels, which strongly depend on nano-Te concentration. In addition, the sample with the highest nano-Te content absorbs light covering 95% of the UV–Vis region, 90% of the near IR region,

and 85% of the far IR region, which may be attributed to the excellent solar absorption of the high-entropy nano-Te and the highly porous architecture of the foam hydrogel (Fig. S10). Additionally, the foam hydrogels are stable to compression, as shown in Figs. 4i and S11.

3.7 Interfacial Evaporation Assessment

The PVA/F-127/nano-Te foam hydrogels were applied as solar evaporators embedded in a commercial black hydrophobic foam deployed as self-floating units on real seawater to examine their heat-supply evaporation behavior, as shown in Figs. 5a and S12. When irradiated under 1 sun, both the PVA/F-127/nano-Te foam hydrogel with 0.37 wt% Te and the surrounding black foam exhibit a gradual increase of temperature over time, where the black foam maintains a much higher temperature (Fig. 5a). Additionally, the interface area B between the sample and the black foam also shows higher temperatures than that of the central area A of the sample. The temperatures are directly proportional to the nano-Te concentrations of the samples, as shown in Fig. 5c, d. The black foam can absorb and transfer light into heat energy, which is partly absorbed by the sample, which has a relatively low temperature. This effect may be helpful for providing additional heating of interfacial water and eliminating in-plane heat loss between the sample and its surroundings. In the absence of the nano-Te samples, the black foam directly heats the central water compared with that without black foam (Fig. 5d). In contrast, when the black foam is replaced with white foam (Fig. S12), which is heat-insulative, the temperatures in areas a, b, and c are all lower than those for the heat-supply model with the same Te content, as shown in Fig. 5b, e. Higher interfacial temperatures are beneficial for desalination by solar evaporators. As shown in Fig. 5f, five typical PVA-based samples were tested for their evaporation capacity under 1 sun relative to bulk water. The samples used were the PVA hydrogel, PVA foam hydrogel, PVA/F-127 foam hydrogel, and the PVA/F-127/nano-Te with 0.37% Te in both heat-supply and heat-insulative models. For the heat-supply model, i.e., the PVA/F-127/nano-Te (black foam) case, the sample showed the best evaporation performance with an average evaporation rate (ν) of 4.11 kg m^{-2} h^{-1} (Fig. 5g) and an average energy efficiency (η) of 128% (Fig. 5h). The addition of F-127 further improves the evaporation rate of the PVA foam hydrogel,

which may be due to the improved homogeneity of bubbles within the PVA foam system (Fig. 5f). Upon varying the Te content of the PVA/F-127/nano-Te samples, both the ν and η values change, with higher values derived from the heat-supply model (Fig. 5h, i). This excellent evaporation performance can be attributed to the evaporation system. First, the present foam hydrogels have lower ΔH_E and higher interfacial temperatures, the latter of which is largely relied on the heat-supply model that provided additional transferred heat energy to the evaporators, giving rise to a higher energy efficiency exceeding 100% [87]. Second, the system provides a hierarchical multiple pore structure that enables fast water transport and water supply.

The combination of these factors imparts the PVA/F-127/nano-Te foam hydrogels with superior performance compared with those of other typical solar evaporators in the literature (Table S1), such as interesting multi-functional fabrics [88–91] and three-dimensional (3D) hydrogels or xerogels [92–94]. Furthermore, our samples also exhibit long-term stability (Fig. 5j). Increasing light intensity further improves the evaporation performance for the thermal isolation model in Fig. 5k. However, this situation was not applicable to the heat-supply model because radiation over 3 suns can damage the black foam through excessive heating.

To explore the potential of the material for practical applications, we prepared a large-scale foam hydrogel and constructed a solar evaporator with the same proportions as those used above (Fig. S13). From September 4, 2022, to October 6, 2022, we monitored the evaporation rate, light intensity, ambient temperature, and central surface temperature of the system for 32 consecutive days of all-day monitoring (Fig. S14). For example, on September 14, 2022, as shown in Fig. 6a, the corresponding ν at different times correlates positively with the light intensity. On this day, the maximum value of ν was 3.11 kg m^{-2} h^{-1} between 11:00 and 12:00 with an average light intensity of 0.905 sun. The measured value of ν decreases at lower light intensity. Figure 6b shows the ion concentrations of the resultant collected water and seawater. After solar desalination, the concentrations of Na$^+$, Mg^{2+}, K$^+$, and Ca^{2+} in the collected water decreased by three orders of magnitude compared with those before desalination. Moreover, no Te-based degradation products are detected, confirming the high purity and safety of the collected water. Furthermore, the solution resistances of several types of water were also measured to evaluate the quality of the collected water, as shown in Figs. 6c and S15.
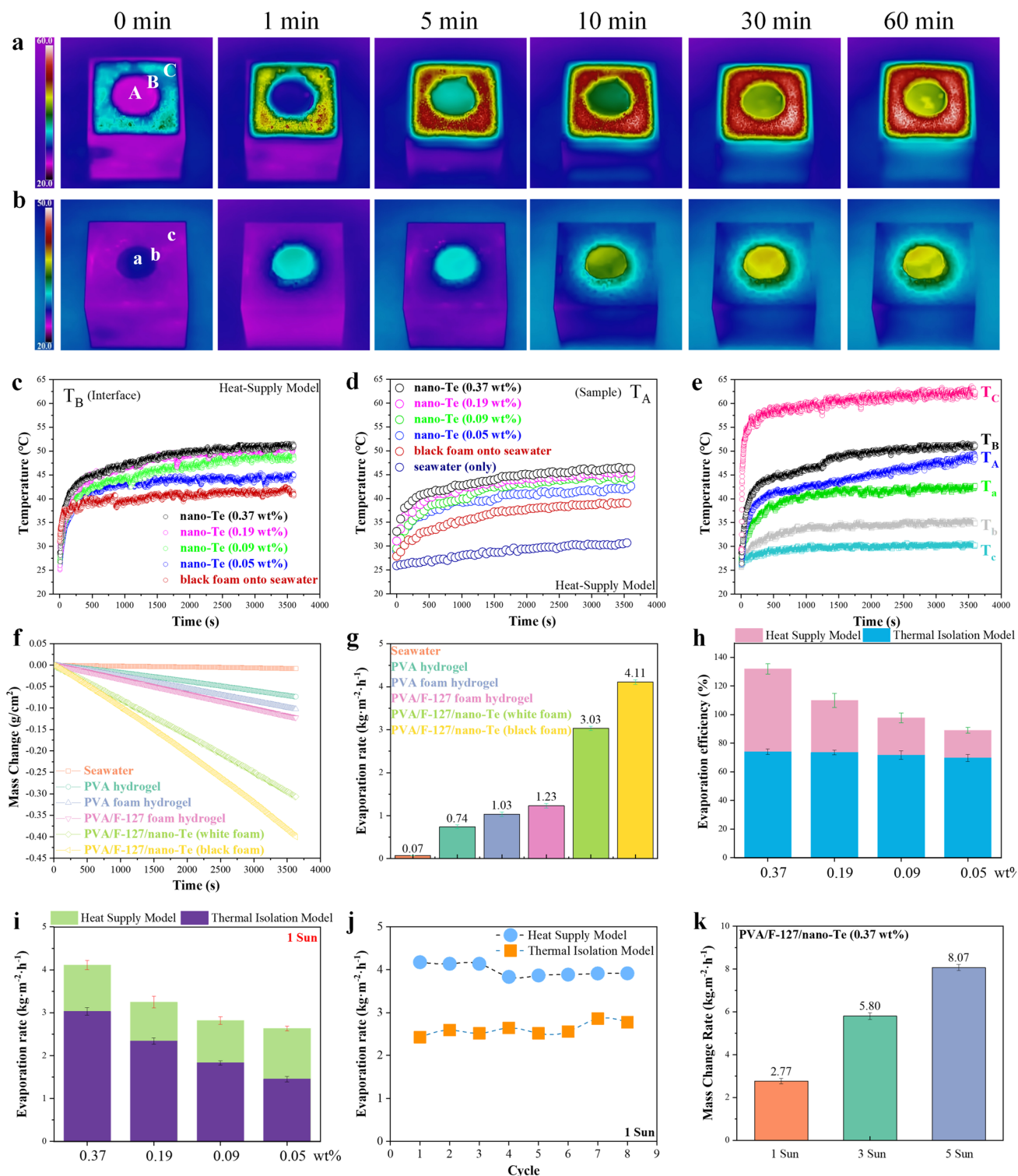
Fig. 5 Solar desalination by foam hydrogels under 1 sun illumination indoors. **a** Thermal image of the heat-supply evaporation model, i.e., foam hydrogel (0.37 wt% Te) embedded into a commercial black foam. **b** Thermal isolation model generated by replacing black with white foam. **c–e** Temperature changes with time for sections A or a (sample central area), B or b (interface between sample and foam), and C or c (foam area distant from sample) for various samples in the above two models. **f** Plots of mass change over time for typical systems and **g** their corresponding evaporation rates (ν). **h, i** Energy efficiency (η) and ν of the PVA/F-127/nano-Te foam hydrogels with various Te concentrations by different models. **j** Evaporation stability of the 0.37 wt% Te sample over eight cycles. **k** Light intensity dependence of ν for the 0.37 wt% Te sample in the thermal isolation model
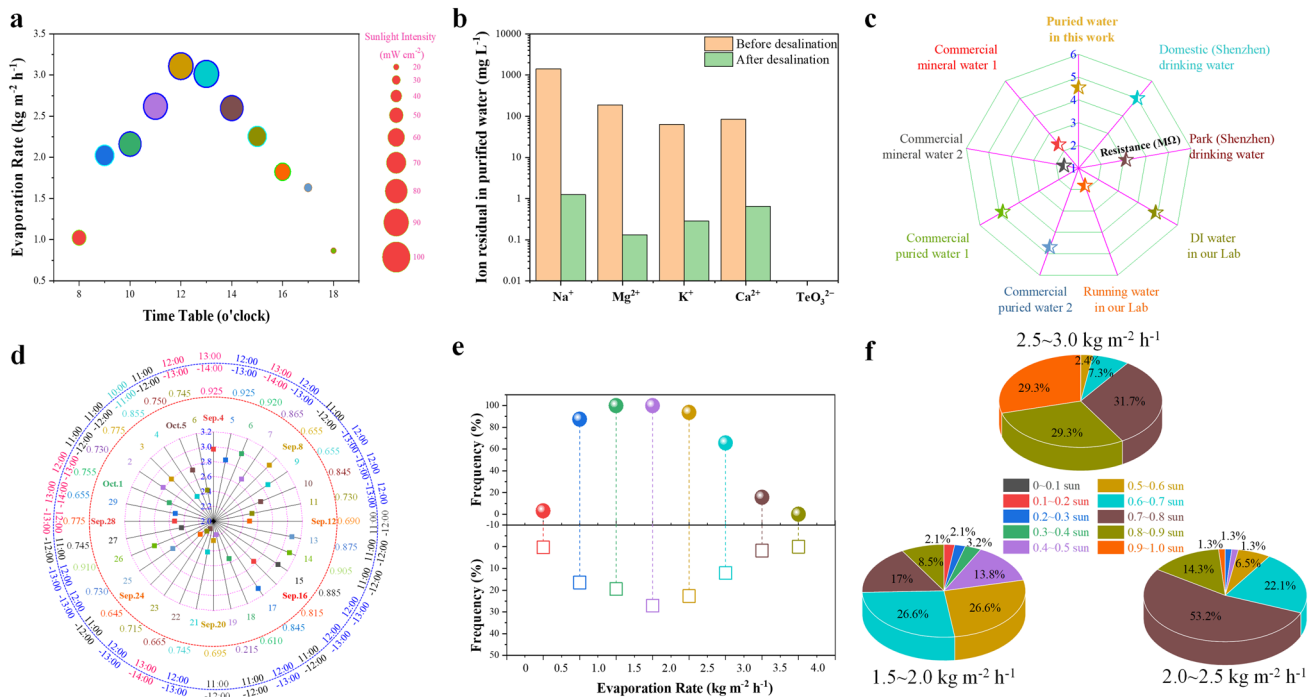
Fig. 6 Solar desalination by the foam hydrogel with 0.37 wt% Te under natural light illumination in the heat-supply model outdoors during September 4 to October 6, 2022. **a** Real-time measurements of ν at different time points on September 14, 2022. Corresponding natural sunlight intensity was also recorded. **b** Ion concentration of real seawater and collected water before and after desalination. **c** Relative resistance of different types of water including seawater, collected water, drinking water, commercial pure water, and mineral water. **d** Maximum daily ν value measured during a 32-day testing period with the corresponding timetable and average light intensity relative to 1 sun. **e** Emergence of specific ν ranges during all days (top) and all the data points (down), including 0–0.5, 0.5–1.0, 1.0–1.5, 1.5–2.0, 2.0–2.5, 2.5–3.0, 3.0–3.5, and 3.5–4.0 kg m^{-2} h^{-1}. **f** Corresponding light intensity region distribution, except for regions of 0–0.5, 0.5–1.0, 1.0–1.5, and 3.5–4.0 kg m^{-2} h^{-1}

Our collected water shows a much higher resistance than tap water and park drinking water, and it is close to that of one of the commercially available purified water samples. In addition, the resistance of the collected water is only slightly lower than that of household drinking water, deionized laboratory water, and another type of commercially available pure water. Thus, the collected water is of high purity and may be drunk or sold directly.

To comprehensively evaluate the real evaporation performance of the sample outdoors, we thoroughly analyzed the 32-day test data and obtained the following results: During September 4 to October 6, the maximum values of ν are in the range 2.2–3.12 kg m^{-2} h^{-1}, made up by 31%, 53%, and 16% of the time in the ranges 2.0–2.5, 2.5–3.0, and > 3.0 kg m^{-2} h^{-1}, respectively. Thus, the evaporation rate is higher than 2.5 kg m^{-2} h^{-1} on approximately 70% of days (Fig. 6d). However, these maximum values are lower than those measured in the laboratory. A possible reason for this difference is that the maximum outdoor light does

not provide the constant 1 sun energy input provided in the laboratory. For example, the maximum average light intensity within the ranges 0.8–0.9 and 0.9–0.95 sun accounts for only 22% and 13%, respectively, reflecting the instability of outdoor radiation. In addition, outdoor temperature and wind speed will affect the final evaporation rate. Evaporation rates in the ranges 0.5–1, 1–1.5, 1.5–2.0, 2.0–2.5, 2.5–3.0, and 3.0–4.0 kg m^{-2} h^{-1} accounted for 16.5%, 19.5%, 27.1%, 22.7%, 12.1%, and 1.7% of the 341 data points recorded, respectively; the corresponding days were 28 days (87.5%), 32 days (100%), 32 days (100%), 30 days (93.7%), 21 days (65.6%), and 5 days (15.6%), respectively (Fig. 6e). The light intensity coincides with the evaporation rate, as shown in Fig. 6f, and the sample maintains a relatively good evaporation rate even under weak sunlight. For example, the evaporation rate is within the range 2.5–3.0 kg m^{-2} h^{-1} (Fig. 6f) under high light intensity (0.8–1.0 sun), which accounted for approximately 60% of the data points, with the remaining 40% accounted for by the range of 0.5–0.8 sun. This value

is even higher than the evaporation performance under the same conditions in the laboratory.

4 Conclusions

The IL [C$_3$NH$_2$MIm][NTf$_2$] can be electrolyzed into active species. The large imidazolium cation breaks down into imidazolium-based radicals that induce rapid swelling of bulk Te and generate an expanded porous structure. Conversely, the small [NTf$_2$] anion of the IL degrades into smaller chemical species that induce fine exfoliation of bulk Te. The as-prepared nano-Te samples had 0D, 1D, and other morphologies, which are beneficial for absorbing solar light over a broad wavelength range at high intensity. The anion-induced nano-Te was terminated by F-, N-, and S-containing chemical groups, whereas only N- and S-containing groups were detected in the case of cation-induced nano-Te. Functionalization of Te can increase local disorder in its atomic arrangement, together with the multiple dimensions, such a strategy can greatly improve solar absorption and photothermal conversion, as revealed by our both experimental and simulation results.

In view of these findings, anion-induced nano-Te was integrated into PVA-based foam hydrogels to construct solar evaporators, which were evaluated under indoor and outdoor conditions. An evaporation rate of 4.11 kg m^{-2} h^{-1} was obtained with a corresponding energy efficiency of 128%. To the best of our knowledge,these are the highest values for semiconductor-based nanocomposites in the literature to date. In outdoor testing, under changing solar irradiation conditions, our solar evaporator exhibited evaporation rates in the range 2.5–3.0 kg m^{-2} h^{-1} under 0.5–1.0 sun. Thus, this study provides a new method for the preparation of functionalized nano-Te and an approach to developing high-performance water evaporation materials that function well under weak light radiation.

Declarations

References

1. Z. He, Y. Yang, J.W. Liu, S.H. Yu, Emerging tellurium nanostructures: controllable synthesis and their applications. Chem. Soc. Rev. **46**(10), 2732–2753 (2017). https://doi.org/10.1039/C7CS00013H

2. Y. Wang, G. Qiu, R. Wang, S. Huang, Q. Wang et al., Field-effect transistors made from solution-grown two-dimensional tellurene. Nat. Electron. **1**(4), 228–236 (2018). https://doi.org/10.1038/s41928-018-0058-4

3. W. Wu, G. Qiu, Y. Wang, R. Wang, P. Ye, Tellurene: its physical properties, scalable nanomanufacturing, and device applications. Chem. Soc. Rev. **47**(19), 7203–7212 (2018). https://doi.org/10.1039/C8CS00598B

4. C. Xing, P. Yin, Z. Peng, H. Zhang, Engineering monochalcogen nanomaterials for omnipotent anticancer applications: progress and challenges. Adv. Healthc. Mater. **9**(14), e2000273 (2020). https://doi.org/10.1002/adhm.202000273

5. G. Qiu, S. Huang, M. Segovia, P.K. Venuthurumilli, Y. Wang et al., Thermoelectric performance of 2d tellurium with accumulation contacts. Nano Lett. **19**(3), 1955–1962 (2019). https://doi.org/10.1021/acs.nanolett.8b05144

6. S. Lin, W. Li, Z. Chen, J. Shen, B. Ge et al., Tellurium as a high-performance elemental thermoelectric. Nat. Commun. **7**(1), 10287 (2016). https://doi.org/10.1038/ncomms10287

7. Z. Shi, R. Cao, K. Khan, A.K. Tareen, X. Liu et al., Two-dimensional tellurium: progress, challenges, and prospects.

Nano-Micro Lett. **12**(1), 99 (2020). https://doi.org/10.1007/s40820-020-00427-z

8. L. Li, J. Kim, C. Jin, G.J. Ye, D.Y. Qiu et al., Direct observation of the layer-dependent electronic structure in phosphorene. Nat. Nanotechnol. **12**(1), 21–25 (2017). https://doi.org/10.1038/nnano.2016.171

9. Z. Guo, S. Chen, Z. Wang, Z. Yang, F. Liu et al., Metal-ion-modified black phosphorus with enhanced stability and transistor performance. Adv. Mater. **29**(42), 1703811 (2017). https://doi.org/10.1002/adma.201703811

10. Z. Sun, H. Xie, S. Tang, X.-F. Yu, Z. Guo et al., Ultrasmall black phosphorus quantum dots: synthesis and use as photothermal agents. Angew. Chem. Int. Ed. **54**(39), 11526–11530 (2015). https://doi.org/10.1002/anie.201506154

11. M. Qiu, D. Wang, W. Liang, L. Liu, Y. Zhang et al., Novel concept of the smart NIR-light–controlled drug release of black phosphorus nanostructure for cancer therapy. Proc. Natl. Acad. Sci. **115**(3), 501–506 (2018). https://doi.org/10.1073/pnas.1714421115

12. Z. Guo, H. Zhang, S. Lu, Z. Wang, S. Tang et al., From black phosphorus to phosphorene: basic solvent exfoliation, evolution of raman scattering, and applications to ultrafast photonics. Adv. Funct. Mater. **25**(45), 6996–7002 (2015). https://doi.org/10.1002/adfm.201502902

13. C. Ma, J. Yan, Y. Huang, C. Wang, G. Yang, The optical duality of tellurium nanoparticles for broadband solar energy harvesting and efficient photothermal conversion. Sci. Adv. **4**(8), eaas9894 (2018). https://doi.org/10.1126/sciadv.aas9894

14. Z. Gao, F. Tao, J. Ren, Unusually low thermal conductivity of atomically thin 2d tellurium. Nanoscale **10**(27), 12997–13003 (2018). https://doi.org/10.1039/c8nr01649f

15. X. Wu, Q. Tao, D. Li, Q. Wang, X. Zhang et al., Unprecedently low thermal conductivity of unique tellurium nanoribbons. Nano Res. **14**(12), 4725–4731 (2021). https://doi.org/10.1007/s12274-021-3414-7

16. S. Huang, M. Segovia, X. Yang, Y.R. Koh, Y. Wang et al., Anisotropic thermal conductivity in 2D tellurium. 2D Mater. **7**(1), 015008 (2020). https://doi.org/10.1088/2053-1583/ab4eee

17. C. Xing, D. Huang, S. Chen, Q. Huang, C. Zhou et al., Engineering lateral heterojunction of selenium-coated tellurium nanomaterials toward highly efficient solar desalination. Adv. Sci. **6**(19), 1900531 (2019). https://doi.org/10.1002/advs.201900531

18. H. Hu, Y. Zeng, S. Gao, R. Wang, J. Zhao et al., Fast solution method to prepare hexagonal tellurium nanosheets for optoelectronic and ultrafast photonic applications. J. Mater. Chem. C **9**(2), 508–516 (2021). https://doi.org/10.1039/D0TC04106H

19. W. Huang, L. He, J. Ouyang, Q. Chen, C. Liu et al., Triangle-shaped tellurium nanostars potentiate radiotherapy by boosting checkpoint blockade immunotherapy. Matter **3**(5), 1725–1753 (2020). https://doi.org/10.1016/j.matt.2020.08.027

20. S. Chen, C. Xing, D. Huang, C. Zhou, B. Ding et al., Eradication of tumor growth by delivering novel photothermal selenium-coated tellurium nanoheterojunctions. Sci. Adv. **6**(15), eaay6825 (2020). https://doi.org/10.1126/sciadv.aay6825

21. K. Wang, Y. Yang, H.W. Liang, J.W. Liu, S.H. Yu, First sub-kilogram-scale synthesis of high quality ultrathin tellurium nanowires. Mater. Horiz. **1**(3), 338–343 (2014). https://doi.org/10.1039/C4MH00004H

22. K. Wang, X. Zhang, I.M. Kislyakov, N. Dong, S. Zhang et al., Bacterially synthesized tellurium nanostructures for broadband ultrafast nonlinear optical applications. Nat. Commun. **10**(1), 3985 (2019). https://doi.org/10.1038/s41467-019-11898-z

23. Y. Choi, T.J. Park, D.C. Lee, S.Y. Lee, Recombinant Escherichia coli as a biofactory for various single- and multi-element nanomaterials. Proc. Natl. Acad. Sci. **115**(23), 5944–5949 (2018). https://doi.org/10.1073/pnas.1804543115

24. Z. Xie, C. Xing, W. Huang, T. Fan, Z. Li et al., Ultrathin 2D nonlayered tellurium nanosheets: facile liquid-phase exfoliation, characterization, and photoresponse with high performance and enhanced stability. Adv. Funct. Mater. **28**(16), 1705833 (2018). https://doi.org/10.1002/adfm.201705833

25. Y. Lin, Y. Wu, R. Wang, G. Tao, P.F. Luo et al., Two-dimensional tellurium nanosheets for photoacoustic imaging-guided photodynamic therapy. Chem. Commun. **54**(62), 8579–8582 (2018). https://doi.org/10.1039/C8CC04653K

26. J. Guo, J. Zhao, D. Huang, Y. Wang, F. Zhang et al., Two-dimensional tellurium–polymer membrane for ultrafast photonics. Nanoscale **11**(13), 6235–6242 (2019). https://doi.org/10.1039/C9NR00736A

27. Q. Wang, M. Safdar, K. Xu, M. Mirza, Z. Wang et al., Van der waals epitaxy and photoresponse of hexagonal tellurium nanoplates on flexible mica sheets. ACS Nano **8**(7), 7497–7505 (2014). https://doi.org/10.1021/nn5028104

28. T. Yang, H. Ke, Q. Wang, Y.A. Tang, Y. Deng et al., Bifunctional tellurium nanodots for photo-induced synergistic cancer therapy. ACS Nano **11**(10), 10012–10024 (2017). https://doi.org/10.1021/acsnano.7b04230

29. J.W. Liu, F. Chen, M. Zhang, H. Qi, C.L. Zhang et al., Rapid microwave-assisted synthesis of uniform ultralong Te nanowires, optical property, and chemical stability. Langmuir **26**(13), 11372–11377 (2010). https://doi.org/10.1021/la100772n

30. N. Yu, J. Li, Z. Wang, S. Yang, Z. Liu et al., Blue Te nanoneedles with strong NIR photothermal and laser-enhanced anticancer effects as "all-in-one" nanoagents for synergistic thermo-chemotherapy of tumors. Adv. Healthc. Mater. **7**(21), 1800643 (2018). https://doi.org/10.1002/adhm.201800643

31. M. Gao, L. Zhu, C.K. Peh, G.W. Ho, Solar absorber material and system designs for photothermal water vaporization towards clean water and energy production. Energy Environ. Sci. **12**(3), 841–864 (2019). https://doi.org/10.1039/C8EE01146J

32. Y. Guo, K. Xu, C. Wu, J. Zhao, Y. Xie, Surface chemical-modification for engineering the intrinsic physical properties of inorganic two-dimensional nanomaterials. Chem. Soc. Rev. **44**(3), 637–646 (2015). https://doi.org/10.1039/C4CS00302K

33. X. Ming, A. Guo, G. Wang, X. Wang, Two-dimensional defective tungsten oxide nanosheets as high performance photo-absorbers for efficient solar steam generation. Sol. Energy Mater. Sol. Cells **185**, 333–341 (2018). https://doi.org/10.1016/j.solmat.2018.05.049

34. A. Ambrosi, M. Pumera, Exfoliation of layered materials using electrochemistry. Chem. Soc. Rev. **47**(19), 7213–7224 (2018). https://doi.org/10.1039/C7CS00811B

35. S. Yang, P. Zhang, A.S. Nia, X. Feng, Emerging 2D materials produced via electrochemistry. Adv. Mater. **32**(10), 1907857 (2020). https://doi.org/10.1002/adma.201907857

36. K. Parvez, Z.S. Wu, R. Li, X. Liu, R. Graf et al., Exfoliation of graphite into graphene in aqueous solutions of inorganic salts. J. Am. Chem. Soc. **136**(16), 6083–6091 (2014). https://doi.org/10.1021/ja5017156

37. J. Lu, J.-X. Yang, J. Wang, A. Lim, S. Wang et al., One-pot synthesis of fluorescent carbon nanoribbons, nanoparticles, and graphene by the exfoliation of graphite in ionic liquids. ACS Nano **3**(8), 2367–2375 (2009). https://doi.org/10.1021/nn900546b

38. A.T. Najafabadi, E.L. Gyenge, High-yield graphene production by electrochemical exfoliation of graphite: novel ionic liquid (IL)–acetonitrile electrolyte with low IL content. Carbon **71**, 58–69 (2014). https://doi.org/10.1016/j.carbon.2014.01.012

39. N. Liu, F. Luo, H. Wu, Y. Liu, C. Zhang et al., One-step ionic-liquid-assisted electrochemical synthesis of ionic-liquid-functionalized graphene sheets directly from graphite. Adv. Funct. Mater. **18**(10), 1518–1525 (2008). https://doi.org/10.1002/adfm.200700797

40. A. Ananthanarayanan, X. Wang, P. Routh, B. Sana, S. Lim et al., Facile synthesis of graphene quantum dots from 3D graphene and their application for Fe^{3+} sensing. Adv. Funct. Mater. **24**(20), 3021–3026 (2014). https://doi.org/10.1002/adfm.201303441

41. X. Tang, H. Chen, J.S. Ponraj, S.C. Dhanabalan, Q. Xiao et al., Fluorination-enhanced ambient stability and electronic tolerance of black phosphorus quantum dots. Adv. Sci. **5**(9), 1800420 (2018). https://doi.org/10.1002/advs.201800420

42. X. Tang, W. Liang, J. Zhao, Z. Li, M. Qiu et al., Fluorinated phosphorene: electrochemical synthesis, atomistic fluorination, and enhanced stability. Small **13**(47), 1702739 (2017). https://doi.org/10.1002/smll.201702739

43. P. Howlett, E. Izgorodina, M. Forsyth, D. Mac-Farlane, Electrochemistry at negative potentials in bis(trifluoromethanesulfonyl)amide ionic liquids. Z. Phys. Chem. **220**, 1483–1498 (2006). https://doi.org/10.1524/zpch.2006.220.10.1483

44. M.C. Kroon, W. Buijs, C.J. Peters, G.J. Witkamp, Decomposition of ionic liquids in electrochemical processing. Green Chem. **8**(3), 241–245 (2006). https://doi.org/10.1039/B512724F

45. E. Markevich, R. Sharabi, V. Borgel, H. Gottlieb, G. Salitra et al., In situ FTIR study of the decomposition of N-butyl-N-methylpyrrolidinium bis(trifluoromethanesulfonyl)amide

46. G.H. Lane, Electrochemical reduction mechanisms and stabilities of some cation types used in ionic liquids and other organic salts. Electrochim. Acta **83**, 513–528 (2012). https://doi.org/10.1016/j.electacta.2012.08.046

47. C.L. Klug, N.J. Bridges, A.E. Visser, S.L. Crump, E. Villa-Aleman, Electrochemical degradation of butyltrimethylammonium bis(trifluoromethylsulfonyl)imide for lithium battery applications. New J. Chem. **38**(8), 3879–3884 (2014). https://doi.org/10.1039/C4NJ00355A

48. R. Michez, T. Doneux, C. Buess-Herman, M. Luhmer, NMR study of the reductive decomposition of [BMIm][NTf$_2$] at gold electrodes and indirect electrochemical conversion of CO_2. ChemPhysChem **18**(16), 2208–2216 (2017). https://doi.org/10.1002/cphc.201700421

49. D. Alwast, J. Schnaidt, K. Hancock, G. Yetis, R.J. Behm, Effect of Li^+ and Mg^{2+} on the electrochemical decomposition of the ionic liquid 1-Butyl-1- methylpyrrolidinium bis(trifluoromethanesulfonyl)imide and related electrolytes. ChemElectroChem **6**(12), 3009–3019 (2019). https://doi.org/10.1002/celc.201900371

50. L. Xiao, K.E. Johnson, Electrochemistry of 1-butyl-3-methyl-1h-imidazolium tetrafluoroborate ionic liquid. J. Electrochem. Soc. **150**(6), E307 (2003). https://doi.org/10.1149/1.1568740

51. M. Forsyth, W.C. Neil, P.C. Howlett, D.R. Macfarlane, B.R. Hinton et al., New insights into the fundamental chemical nature of ionic liquid film formation on magnesium alloy surfaces. ACS Appl. Mater. Interfaces **1**(5), 1045–1052 (2009). https://doi.org/10.1021/am900023j

52. A.S. Ismail, S.Z. El Abedin, O. Höfft, F. Endres, Unexpected decomposition of the bis (trifluoromethylsulfonyl) amide anion during electrochemical copper oxidation in an ionic liquid. Electrochem. Commun. **12**(7), 909–911 (2010). https://doi.org/10.1016/j.elecom.2010.04.018

53. P.C. Howlett, N. Brack, A.F. Hollenkamp, M. Forsyth, D.R. MacFarlane, Characterization of the lithium surface in N-methyl-N-alkylpyrrolidinium bis(trifluoromethanesulfonyl) amide room-temperature ionic liquid electrolytes. J. Electrochem. Soc. **153**(3), A595 (2006). https://doi.org/10.1149/1.2164726

54. Q. Xiao, X.-Y. Li, Z.-Q. Zhang, C.-X. Hu, G.-H. Dun et al., Facile fabrication of highly uniform tellurium nanorods for self-powered flexible optoelectronics. Adv. Electron. Mater. **6**(7), 2000240 (2020). https://doi.org/10.1002/aelm.202000240

55. G. Kresse, J. Furthmüller, Efficient iterative schemes for ab initio total-energy calculations using a plane-wave basis set. PhRvB **54**(16), 11169–11186 (1996). https://doi.org/10.1103/PhysRevB.54.11169

56. J.P. Perdew, K. Burke, M. Ernzerhof, Generalized gradient approximation made simple. Phys. Rev. Lett. **77**(18), 3865–3868 (1996). https://doi.org/10.1103/PhysRevLett.77.3865

57. P.E. Blöchl, Projector augmented-wave method. PhRvB **50**(24), 17953–17979 (1994). https://doi.org/10.1103/PhysRevB.50.17953

58. M.C. Payne, M.P. Teter, D.C. Allan, T.A. Arias, J.D. Joannopoulos, Iterative minimization techniques for ab initio total-energy calculations: molecular dynamics and conjugate gradients. Rev. Mod. Phys. **64**(4), 1045–1097 (1992). https://doi.org/10.1103/RevModPhys.64.1045

59. J. Moellmann, S. Grimme, Dft-d3 study of some molecular crystals. J. Phys. Chem. C **118**(14), 7615–7621 (2014). https://doi.org/10.1021/jp501237c

60. W.W. Gärtner, Photothermal effect in semiconductors. Phys. Rev. **122**(2), 419–424 (1961). https://doi.org/10.1103/PhysRev.122.419

61. S.I. Ibrahim, A.H. Ali, S.A. Hafidh, M.T. Chaichan, H.A. Kazem et al., Stability and thermal conductivity of different nano-composite material prepared for thermal energy storage applications. South Afr. J. Chem. Eng. **39**, 72–89 (2022). https://doi.org/10.1016/j.sajce.2021.11.010

62. Convective Heat Transfer. Engineering ToolBox, (2003). [online]. https://www.engineeringtoolbox.com/convective-heat-transfer-d_430.html

63. X. Wang, R. Guo, Q. Jian, G. Peng, Y. Yue et al., Thermal characterization of convective heat transfer in microwires based on modified steady state "hot wire" method. arXiv:1907.10751 (2019). https://doi.org/10.48550/arXiv.1907.10751

64. N. Dewan, K. Sreenivas, V. Gupta, Properties of crystalline γ-TeO$_2$ thin film. J. Cryst. Growth **305**(1), 237–241 (2007). https://doi.org/10.1016/j.jcrysgro.2007.03.054

65. H.H. Wei, J. Lin, W.H. Huang, Z.B. Feng, D.-W. Li, Preparation of TeO$_2$ based thin films by nonhydrolytic sol–gel process. Mater. Sci. Eng. B **164**(1), 51–59 (2009). https://doi.org/10.1016/j.mseb.2009.07.001

66. B. Qin, Y. Bai, Y. Zhou, J. Liu, X. Xie et al., Structure and characterization of TeO$_2$ nanoparticles prepared in acid medium. Mater. Lett. **63**(22), 1949–1951 (2009). https://doi.org/10.1016/j.matlet.2009.06.018

67. C.W. Liew, S. Ramesh, R. Durairaj, Impact of low viscosity ionic liquid on PMMA-PVC-LiTFSI polymer electrolytes based on AC-impedance, dielectric behavior, and HATR-FTIR characteristics. J. Mater. Res. **27**(23), 2996–3004 (2012). https://doi.org/10.1557/jmr.2012.343

68. T. Moumene, E.H. Belarbi, B. Haddad, D. Villemin, O. Abbas et al., Vibrational spectroscopic study of ionic liquids: comparison between monocationic and dicationic imidazolium ionic liquids. J. Molecular Struct. **1065–1066**, 86–92 (2014). https://doi.org/10.1016/j.molstruc.2014.02.034

69. W.Q. Feng, Y.H. Lu, Y. Chen, Y.W. Lu, T. Yang, Thermal stability of imidazolium-based ionic liquids investigated by TG and FTIR techniques. J. Therm. Anal. Calorim. **125**(1), 143–154 (2016). https://doi.org/10.1007/s10973-016-5267-3

70. S.A. Katsyuba, E.E. Zvereva, A. Vidiš, P.J. Dyson, Application of density functional theory and vibrational spectroscopy toward the rational design of ionic liquids. J. Phys. Chem. A **111**(2), 352–370 (2007). https://doi.org/10.1021/jp064610i

71. J. Kiefer, J. Fries, A. Leipertz, Experimental vibrational study of imidazolium-based ionic liquids: Raman and infrared spectra of 1-ethyl-3-methylimidazolium bis(trifluoromethylsulfonyl)imide and 1-ethyl-3-methylimidazolium ethylsulfate. Appl. Spectrosc. **61**(12), 1306–1311 (2007). https://doi.org/10.1366/000370207783292000

72. S. Men, K.R.J. Lovelock, P. Licence, X-ray photoelectron spectroscopy of pyrrolidinium-based ionic liquids: cation–anion interactions and a comparison to imidazolium-based analogues. Phys. Chem. Chem. Phys. **13**(33), 15244–15255 (2011). https://doi.org/10.1039/C1CP21053J

73. A. Rezaei, L. Hadian-Dehkordi, H. Samadian, M. Jaymand, H. Targhan et al., Pseudohomogeneous metallic catalyst based on tungstate-decorated amphiphilic carbon quantum dots for selective oxidative scission of alkenes to aldehyde. Sci. Rep. **11**(1), 4411 (2021). https://doi.org/10.1038/s41598-021-83863-0

74. Z. Dong, L. Zhao, Covalently bonded ionic liquid onto cellulose for fast adsorption and efficient separation of Cr(VI): batch, column and mechanism investigation. Carbohydr. Polym. **189**, 190–197 (2018). https://doi.org/10.1016/j.carbpol.2018.02.038

75. Y. Tang, Z. Wang, X. Chi, M.D. Sevilla, X. Zeng, In situ generated platinum catalyst for methanol oxidation via electrochemical oxidation of bis(trifluoromethylsulfonyl)imide anion in ionic liquids at anaerobic condition. J. Phys. Chem. C **120**(2), 1004–1012 (2016). https://doi.org/10.1021/acs.jpcc.5b09777

76. Y. Tang, L. Lin, A. Kumar, M. Guo, M. Sevilla et al., Hydrogen electrooxidation in ionic liquids catalyzed by the NTf(2) radical. J. Phys. Chem. C Nanomater. Interfaces **121**(9), 5161–5167 (2017). https://doi.org/10.1021/acs.jpcc.7b00335

77. N. DeVos, C. Maton, C.V. Stevens, Electrochemical stability of ionic liquids: general influences and degradation mechanisms. ChemElectroChem **1**(8), 1258–1270 (2014). https://doi.org/10.1002/celc.201402086

78. Q.X. Liu, S. Zein El Abedin, F. Endres, Electrodeposition of nanocrystalline aluminum: breakdown of imidazolium cations modifies the crystal size. J. Electrochem. Soc. **155**(5), D357 (2008). https://doi.org/10.1149/1.2884369

79. P.A. Hunt, C.R. Ashworth, R.P. Matthews, Hydrogen bonding in ionic liquids. Chem. Soc. Rev. **44**(5), 1257–1288 (2015). https://doi.org/10.1039/C4CS00278D

80. K. Dong, S. Zhang, J. Wang, Understanding the hydrogen bonds in ionic liquids and their roles in properties and reactions. Chem. Commun. **52**(41), 6744–6764 (2016). https://doi.org/10.1039/C5CC10120D

81. J. Kruusma, T. Käämbre, A. Tõnisoo, V. Kisand, K. Lust et al., The electrochemical behaviour of butyltrimethylammonium bis(trifluoromethylsulfonyl)imide at negatively polarised aluminium electrode studied by in situ soft X-ray photoelectron spectroscopy, electrochemical impedance spectroscopy and cyclic voltammetry techniques. J. Solid State Electrochem. **26**(12), 2805–2815 (2022). https://doi.org/10.1007/s10008-022-05281-0

82. Y. Zhou, Y.Z. Zheng, T. Zhang, G. Deng, Z.W. Yu, Evidence that acetonitrile is sensitive to different interaction sites of ionic liquids as revealed by excess spectroscopy. ChemPhysChem **18**(10), 1370–1375 (2017). https://doi.org/10.1002/cphc.201601376

83. Y. Zhou, S. Gong, X. Xu, Z. Yu, J. Kiefer et al., The interactions between polar solvents (methanol, acetonitrile, dimethylsulfoxide) and the ionic liquid 1-ethyl-3-methylimidazolium bis(fluorosulfonyl)imide. J. Mol. Liquids **299**, 112159 (2020). https://doi.org/10.1016/j.molliq.2019.112159

84. Y.Z. Zheng, N.N. Wang, J.J. Luo, Y. Zhou, Z.W. Yu, Hydrogen-bonding interactions between [BMIM][BF$_4$] and acetonitrile. Phys. Chem. Chem. Phys. **15**(41), 18055–18064 (2013). https://doi.org/10.1039/C3CP53356E

85. Y. Lauw, M.D. Horne, T. Rodopoulos, V. Lockett, B. Akgun et al., Structure of [C4mpyr][NTf$_2$] room-temperature ionic liquid at charged gold interfaces. Langmuir **28**(19), 7374–7381 (2012). https://doi.org/10.1021/la3005757

86. Y. Guo, L.S. de Vasconcelos, N. Manohar, J. Geng, K.P. Johnston, G. Yu, Highly elastic interconnected porous hydrogels through self-assembled templating for solar water purification. Angew. Chem. Int. Ed. **61**(3), e202114074 (2022). https://doi.org/10.1002/anie.202114074

87. C. Xing, Z. Li, S. Zhang, J. Bang, Z. Xie et al., Phase inversion-based foam hydrogels for highly efficient solar-powered interfacial desalination. Chem. Eng. J. **464**, 142409 (2023). https://doi.org/10.1016/j.cej.2023.142409

88. S. Sun, H. Li, M. Zhang, B. Sun, Y. Xie et al., A multifunctional asymmetric fabric for sustained electricity generation from multiple sources and simultaneous solar steam generation. Small (2023). https://doi.org/10.1002/smll.202303716

89. S. Sun, Q. Tian, H.-Y. Mi, J. Li, X. Jing et al., Fabric-based all-weather-available photo-electro-thermal steam generator with high evaporation rate and salt resistance. Sci. China Mater. **65**(9), 2479–2490 (2022). https://doi.org/10.1007/s40843-021-2010-1

90. S. Sun, Y. Wang, B. Sun, F. Zhang, Q. Xu et al., Versatile janus composite nonwoven solar absorbers with salt resistance for efficient wastewater purification and desalination. ACS Appl. Mater. Interfaces **13**(21), 24945–24956 (2021). https://doi.org/10.1021/acsami.1c05618

91. S. Sun, B. Sun, Y. Wang, M. Fordjour Antwi-Afari, H.-Y. Mi et al., Carbon black and polydopamine modified non-woven fabric enabling efficient solar steam generation towards seawater desalination and wastewater purification. Sep. Purif. Technol. **278**, 119621 (2021). https://doi.org/10.1016/j.seppur.2021.119621

92. J. Ren, L. Chen, J. Gong, J. Qu, R. Niu, Hofmeister effect mediated hydrogel evaporator for simultaneous solar evaporation and thermoelectric power generation. Chem. Eng. J. **458**, 141511 (2023). https://doi.org/10.1016/j.cej.2023.141511

93. L. Chen, J. Ren, J. Gong, J. Qu, R. Niu, Cost-effective, scalable fabrication of self-floating xerogel foam for simultaneous photothermal water evaporation and thermoelectric power generation. Chem. Eng. J. **454**, 140383 (2023). https://doi.org/10.1016/j.cej.2022.140383

94. P. He, H. Lan, H. Bai, Y. Zhu, Z. Fan et al., Rational construction of "all-in-one" metal-organic framework for integrated solar steam generation and advanced oxidation process. Appl. Catal. B-Environ. **337**, 123001 (2023). https://doi.org/10.1016/j.apcatb.2023.123001